

# Multiscale photoacoustic microscopy and computed tomography

Lihong V. Wang<sup>1</sup>

**Photoacoustic tomography (PAT) is probably the fastest-growing area of biomedical imaging technology, owing to its capacity for high-resolution sensing of rich optical contrast *in vivo* at depths beyond the optical transport mean free path (~1 mm in human skin). Existing high-resolution optical imaging technologies, such as confocal microscopy and two-photon microscopy, have had a fundamental impact on biomedicine but cannot reach the penetration depths of PAT. By utilizing low ultrasonic scattering, PAT indirectly improves tissue transparency up to 1000-fold and consequently enables deeply penetrating functional and molecular imaging at high spatial resolution. Furthermore, PAT promises *in vivo* imaging at multiple length-scales; it can image subcellular organelles to organs with the same contrast origin — an important application in multiscale systems biology research.**

Photoacoustic tomography<sup>1–3</sup>, also referred to as optoacoustic tomography, is the cross-sectional or three-dimensional (3D) imaging of a material using the photoacoustic effect. Planar imaging without depth resolution or one-dimensional (1D) depth-resolved imaging does not belong to this field. In the photoacoustic phenomenon, light is absorbed by a material and converted to heat, and the subsequent thermoelastic expansion generates an acoustic wave. PAT — a hybrid of optical imaging and ultrasound imaging — combines rich optical contrast and high ultrasonic resolution in a single modality. It provides high-resolution structural, functional<sup>4–7</sup> and molecular<sup>8–13</sup> imaging *in vivo* in optically scattering biological tissue at unprecedented depths. Although structural imaging cannot differentiate between live and dead tissue, functional imaging can by measuring physiological functions such as blood flow and oxygenation. Furthermore, molecular imaging can sense biomarkers to identify specific cancer cells or detect gene expression products to track gene activations. One hundred years after Bell reported the photoacoustic effect in 1880 (ref. 14), Bowen envisaged its potential for imaging by excitation using both ionizing radiation (high-energy electrons, X-ray photons, neutrons and other charged particles) and non-ionizing radiation (radio waves, microwaves and ultrasonic waves)<sup>15</sup>. He demonstrated 1D depth-resolved imaging using radio-wave excitation, but did not discuss the possibility of using optical excitation. As a precursor to PAT, laser-induced photoacoustic depth-resolved imaging was achieved, although there was very little (~6 mm) lateral resolution in the direction perpendicular to the acoustic axis<sup>16–20</sup>. To obtain cross-sectional or 3D images that are resolved both axially and laterally, PAT based on an approximate reconstruction algorithm was developed<sup>21</sup>. In addition, PAT based on tightly focused ultrasonic detection was attained<sup>22</sup>. In 2003, *in vivo* functional PAT was reported<sup>4</sup> — this article highlights the subsequent rapid growth of research.

Although many biomedical imaging modalities exist, their limitations call for new imaging technologies. Optical imaging is a strong contender, primarily because of its rich contrast. From a safety perspective, it is non-ionizing radiation with photon energy ~2 eV, making it much safer than X-rays (which have photon energy of thousands of eV and can consequently cause carcinogenesis). From a physics perspective, optical signals are related to the molecular constituents of tissue and hence can provide biochemical information that reflects the physiological state. From an optics perspective, optical absorption is related to various intrinsic contrast origins, such as oxygenated and deoxygenated haemoglobin, melanin, lipids,

and even water. As a result, optical imaging can provide functional imaging to map physiological parameters. By using multiwavelength measurement, one can simultaneously quantify concentrations of multiple chromophores of different colours (for example, oxygenated and deoxygenated haemoglobin molecules in red blood cells). Such quantification can provide functional imaging of the concentration and the oxygen saturation of haemoglobin — both of which are related to angiogenesis and hypermetabolism (hallmarks of cancer) — as well as brain activity or injuries<sup>4,23,24</sup>. Furthermore, extrinsic optical absorption contrast agents can be used to provide molecular imaging of gene expressions or biomarkers<sup>8–13</sup>.

## Diffraction and diffusion challenges in optical imaging

High-resolution optical microscopy faces two fundamental challenges: diffraction and diffusion. Diffraction limits the spatial resolution, whereas diffusion limits the penetration depth. Recently, the resolution of optical microscopy has been improved beyond the diffraction limit and is covered well elsewhere<sup>25–27</sup>; this article focuses on the breaking of the diffusion limit.

Despite light diffusion from tissue scattering, shining a torch through the palm or fingers demonstrates the penetration capability of scattered light in biological tissue. However, although torchlight is broadband, only red light is transmitted substantially. Unlike X-ray photons, optical photons do not cast a shadow of the bone, a feature that is well-understood in biomedical optics. Haemoglobin — the primary chromophore in biological tissue — absorbs light strongly in the green and blue spectral regions, allowing red light to propagate further than shorter-wavelength light before being absorbed. Furthermore, strong scattering of light by tissue components such as cell nuclei and mitochondria blurs any shadows of internal structure. In fact, a red photon may experience hundreds or thousands of scattering events before being absorbed. The reciprocal of the mean distance between equivalent isotropic scattering events — the transport mean free path — is approximately 1 mm for visible and near-infrared light. Below this depth, the description of photon propagation changes from the ballistic regime to the diffusive regime<sup>28</sup>. Because optical focusing is ineffective in the diffusive regime, the transport mean free path is referred to as ‘the soft-depth limit for high-resolution optical imaging’. Beyond this limit, no purely optical imaging technologies have been able to achieve high spatial resolution. Although scattering alone does not eliminate photons, longer photon paths increase the chance of tissue

<sup>1</sup>Optical Imaging Laboratory, Department of Biomedical Engineering, Washington University in St. Louis, Campus Box 1097, One Brookings Drive, St. Louis, Missouri 63130-4899, USA. e-mail: lhwang@biomed.wustl.edu

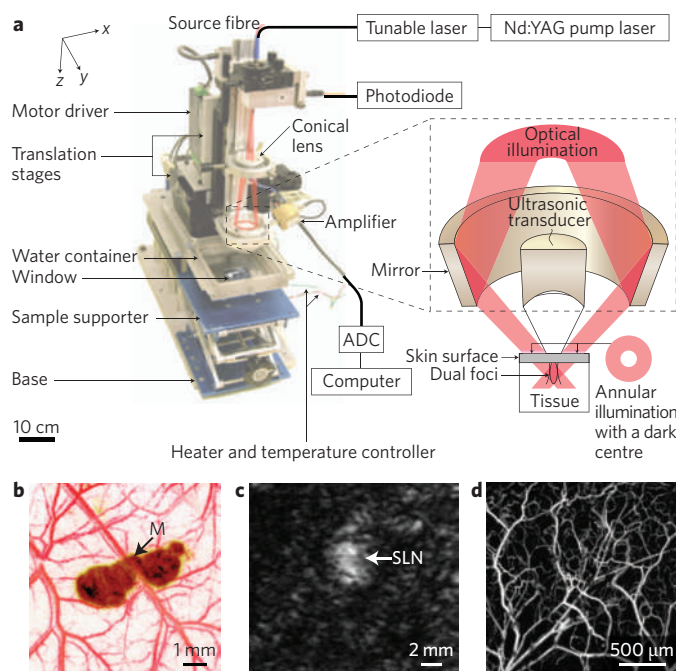


**Figure 1 | Multiscale scanning photoacoustic imaging of small animals *in vivo*.** **a**, Dark-field confocal photoacoustic microscope. ADC, analog-to-digital converter. **b**, Photoacoustic image of a melanoma and blood vessels acquired with a 50-MHz photoacoustic microscope at an axial resolution of 15  $\mu\text{m}$  and a penetration limit of 3 mm. M, melanoma. **c**, Photoacoustic image of a sentinel lymph node (SLN) 18 mm below the laser-illumination surface, acquired with a 5-MHz photoacoustic macroprobe at an axial resolution of 144  $\mu\text{m}$  and a penetration limit of 30 mm. **d**, Photoacoustic image of the vasculature (including capillaries), acquired with an optical-resolution photoacoustic microscope, at a lateral resolution of 5  $\mu\text{m}$  and a penetration limit of 0.7 mm. Images in **a** and **b** are reproduced with permission from ref. 32. © 2006 NPG. Image in **c** is reproduced from ref. 50. © 2008 SPIE.

absorption. Even diffuse photons are too few to be practically useful beyond a depth of  $\sim 50$  mm, referred to as ‘the hard-depth limit for optical imaging’.

PAT overcomes the soft-depth limit and achieves deep imaging at high resolution. The ultrasonic scattering coefficient in tissue is 2–3 orders of magnitude less than the optical equivalent. As a result, PAT can provide high spatial resolution by detecting ultrasonic waves induced by diffuse photons. In most cases, the centre frequency and the bandwidth of the ultrasonic detection system are the main determinants of spatial resolution; a higher centre frequency and wider bandwidth increase spatial resolution but decrease penetration depth. Such scalability allows for multiscale imaging. It is also worth mentioning that lower-frequency electromagnetic waves, including microwaves and radio waves, have been adopted for photoacoustic excitation to overcome the optical hard-depth limit<sup>29,30</sup>.

Although ultrasound imaging can provide high spatial resolution, speckle artefacts cause the images to appear grainy. The relative spatial resolution — defined as the ratio of the penetration limit to the depth resolution; that is, the pixel count in the depth direction without artificial interpolation — is more than 100, considered high enough to provide good-quality images. PAT inherits the high spatial resolution of ultrasound imaging without the issue of speckle formation. As all initial photoacoustic pressure rises are positive, there are strong correlations between the photoacoustic waves from the absorbers. Consequently, prominent boundaries always build up in photoacoustic images and suppress the interior fluctuations, making PAT speckle-free<sup>31</sup>.

## Fundamentals of PAT

When PAT is expressed in simple terms, light goes in and ultrasound comes out. A short-pulsed laser is normally used for efficient ultrasound generation. The strength of the photoacoustic pressure depends on the optical energy deposition as well as the thermal and mechanical properties of the tissue. As long as the photons are converted into heat, either scattered or unscattered photons can produce photoacoustic signals and allow PAT to function in the optical diffusive regime. Image formation is essentially a triangulation of the photoacoustic sources according to the time-of-flight signals recorded at multiple locations outside the tissue<sup>2,28</sup>.

PAT has two major modes: focused scanning tomography and computed tomography. In focused scanning PAT, such as dark-field confocal photoacoustic microscopy (PAM)<sup>32,33</sup>, a focused ultrasonic transducer is scanned mechanically<sup>29</sup>. At each scanned position, the acoustic focusing yields lateral resolution and the acoustic time-of-flight provides axial resolution. In photoacoustic computed tomography, an array of unfocused ultrasonic transducers detects photoacoustic waves in parallel, allowing high frame rates ( $\sim 50$  Hz) to be achieved<sup>3,4,21,34–46</sup>. However, an inverse reconstruction algorithm is required to reconstruct the tomographic image. Early reconstructions were based on the assumption that each ultrasonic transducer receives signals simultaneously from photoacoustic sources on a plane instead of a spherical surface<sup>21</sup>, which can be difficult to achieve in practice. Various groups then developed more accurate reconstruction algorithms<sup>3</sup>. More recently, an exact closed-form reconstruction formula was found for three detection geometries: planar, cylindrical and spherical<sup>41</sup>. Interestingly, one may think of a focused ultrasonic transducer used in the focused scanning mode as an analogue computer that performs approximately the inverse algorithm in the computed tomography mode. Although hardware focusing does not introduce discretization artefacts, the focal position can be adjusted more readily in photoacoustic computed tomography. As a result, optimal lateral resolution is achievable only within the focal zone unless a synthetic aperture algorithm based on a virtual detector is used.

PAT is extremely sensitive to optical absorption. The photoacoustic excitation converts a small change in optical absorption coefficient to a fractionally equal change in ultrasound signal. For the same reason, PAT is also sensitive to any change in the Grüneisen coefficient (the conversion efficiency of optical energy deposition to pressure), which can also provide image contrast. In particular, the Grüneisen coefficient increases with equilibrium temperature (for example,  $\sim 5\%$  per Kelvin in water), enabling PAT to image temperature with a sensitivity of 0.16  $^{\circ}\text{C}$  — useful for monitoring thermal therapy<sup>47–49</sup>.

In soft tissue, a laser-induced temperature rise of 1 mK yields an initial pressure of  $\sim 800$  Pa, which is similar to the sensitivities of typical ultrasonic transducers. The conversion of temperature rise to pressure is related by two parameters: volume expansion coefficient and compressibility. Fortunately, these two parameters combine to create safe temperature rises that allow PAT to be safely used in live tissue.

## Multiscale photoacoustic microscopy

Dark-field confocal PAM can image optical absorption contrast at depths beyond the optical transport mean free path, with a ratio of penetration limit to depth resolution of greater than 100 (Fig. 1a)<sup>32,33</sup>. For ease of system operation, an optical fibre is used to deliver the excitation laser light, which is monitored by a photodiode for energy calibration. A conical lens is used to form a toroidal beam (annular illumination with a dark centre; that is, dark field) to minimize the effect of surface photoacoustic signals on the deeper signals. The beam is then weakly focused into the tissue while the ultrasonic transducer focuses coaxially into the same region for confocal excitation and detection. The photoacoustic time-of-flight signal is recorded at each location of the ultrasonic transducer. By assuming the speed of sound

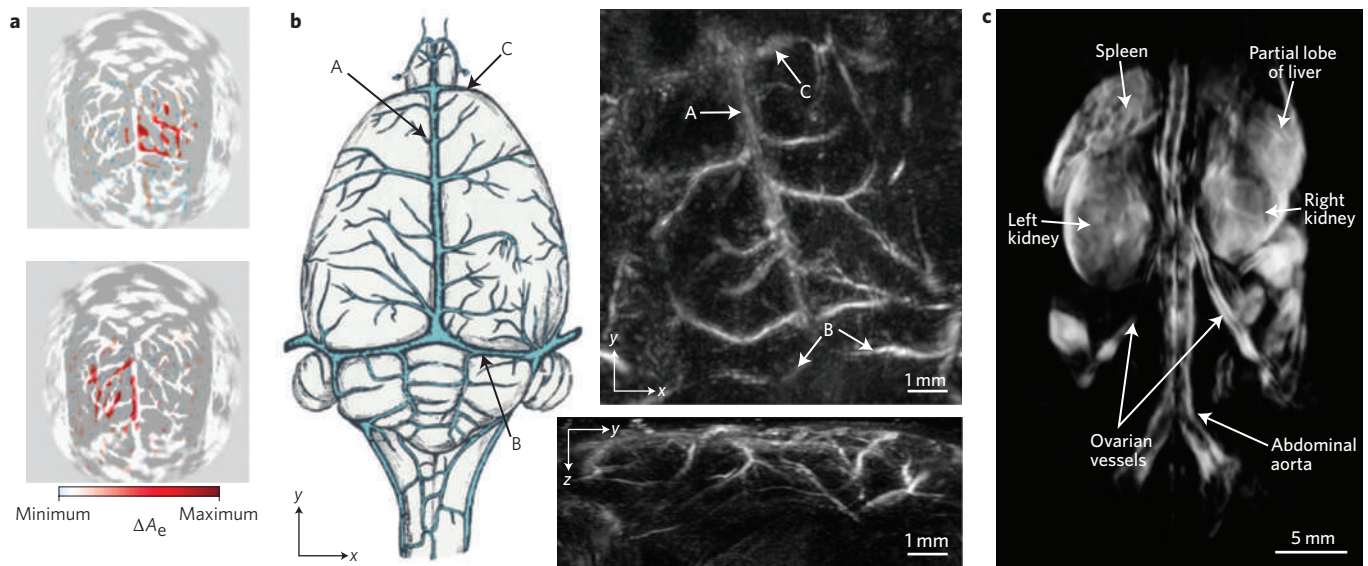


**Figure 2 | Non-invasive photoacoustic computed tomography of small animals.** **a**, Functional images of a rat brain acquired *in vivo* with left- and right-side whisker stimulations, respectively. The colour scale shows differential absorption  $\Delta A_e$  due to brain activation, and the grey shows the structure of the cortex. The field of view is 20 mm  $\times$  20 mm. **b**, Schematic representation of superficial cerebral vascular anatomy (left) and images of a mouse acquired *ex vivo* with a system based on Fabry–Pérot interferometry. A, superior sagittal sinus; B, lateral sinus; C, inferior cerebral vein. **c**, Whole-body image of a mouse acquired *in vivo*. A 10-mm-thick section of the abdomen is shown. Images in **a**, **b** and **c** are reproduced from, respectively, ref. 4. © 2003 NPG; ref. 68. © 2009 OSA; and ref. 71. © 2009 SPIE.

to be 1.54 mm  $\mu\text{s}^{-1}$ , the time-of-flight is converted into depth and consequently a 1D depth-resolved image called an ‘A-line’ is formed. Linear or raster scanning over the tissue produces two-dimensional (2D) or 3D tomographic images, respectively. Here, the broadband ultrasonic detector has a numerical aperture of 0.44 and a centre frequency of 50 MHz. As a result, the lateral resolution, determined by the focal diameter of the ultrasonic transducer at the centre frequency, was  $\sim 45 \mu\text{m}$ . The axial resolution, determined by the ultrasonic bandwidth, was  $\sim 15 \mu\text{m}$ . The maximum imaging depth, determined by the ultrasonic attenuation in tissue, was  $>3 \text{ mm}$  (refs 32,33). A representative PAM image is shown in Fig. 1b.

The image resolution and the penetration limit are scalable with the ultrasonic frequency. For example, a 5-MHz ultrasonic transducer and an 804-nm near-infrared light source scaled the penetration to 30 mm and the resolution to 144  $\mu\text{m}$  and 560  $\mu\text{m}$  in the axial and lateral directions, respectively<sup>50</sup>. The near-infrared window is conducive for deep imaging because of the low level of haemoglobin absorption. Here, photoacoustic microscopy becomes macroscopy, and can potentially provide penetration up to the hard-depth limit ( $\sim 50 \text{ mm}$ ) at  $<1 \text{ mm}$  resolution. Such a system could image deep human tissue such as the sentinel lymph node (SLN), which has an average depth of  $12 \pm 5 \text{ mm}$  in ultrasound images<sup>50</sup>. An *in vivo* image of a rat overlaid with additional tissue was acquired with this system (Fig. 1c), where the SLN accumulated injected dye through the lymphatic system<sup>50</sup>. This imaging capability, followed by needle biopsy, can potentially transform SLN mapping — used for breast cancer staging — from a surgical procedure into a minimally invasive procedure.

The spatial resolution of the original PAM system can also be scaled down. Focusing light through an objective lens with a numerical aperture of 0.1 yields a lateral resolution of 5  $\mu\text{m}$  that is limited by the optical focal diameter. Such a resolution allows *in vivo* imaging of capillaries — the smallest blood vessels — where single files of red blood cells are imaged (Fig. 1d). In this work<sup>51</sup>, light delivery and ultrasonic detection are merged using a beam combiner, although this can also be done using a ring ultrasonic transducer described earlier<sup>52</sup>. Increasing the numerical aperture allows potentially sub-micrometre resolution to be achieved, although optical focusing is

still effective only within the soft-depth limit<sup>28</sup>; so far, a penetration of 0.7 mm has been achieved.

Multiscale systems biology, recognized as an important future direction in biomedical science, needs the support of *in vivo* multiscale imaging with common signal origins. To understand the workings of an entire biological system, biological components spanning multiple spatial scales — from subcellular organelles (sub-micrometre scale) to cells (micrometre scale) and organs (centimetre scale) — must be integrated. As discussed above, photoacoustic microscopy and macroscopy are uniquely capable of such multiscale imaging with the same contrast mechanism of optical absorption.

Photoacoustic sensing has recently been shown to be capable of detecting single melanoma cells *in vivo* in the lymph vessels of small animals<sup>53</sup>. This technology, coined ‘*in vivo* photoacoustic flow cytometry’, may allow *in vivo* detection of circulating tumour cells in humans. Cells flowing through a lymph valve are focused naturally into a single file, facilitating single-cell detection in the lymph vessel. The transparency of the lymph presents low background noise and consequently allows for high-sensitivity detection. Melanin in the melanoma cells provides high optical absorption for photoacoustic detection without the use of exogenous labelling, which can be toxic. Exogenous contrast agents can, however, be used to provide molecular specificity for targeted biomarkers<sup>53</sup>. Several optical wavelengths can be used to detect multiple cell types with different characteristic optical absorption spectra. In humans, it was suggested that superficial lymphatics in the leg be targeted first<sup>54</sup>. The concept can also be applied to blood vessels, although background from erythrocytes can compete with signals from other absorbers<sup>55–58</sup>. At present, the technology is limited to non-imaging sensing; however, there is potential for PAM to be used for imaging purposes.

### Photoacoustic computed tomography

In circular-view photoacoustic computed tomography, ultrasonic detection follows a ring<sup>4,59,60</sup>. A pulsed laser beam is expanded to illuminate the object and an ultrasonic transducer scans around the object in a circle to acquire the photoacoustic data. An inverse algorithm then converts the photoacoustic data to the initial photoacoustic pressure distribution, which is an image of the cross-section

containing the scanned circle. Representative functional images are shown in Fig. 2a. The ultrasonic transducer has a broad bandwidth centred at 3.5 MHz, yielding an in-plane resolution of  $\sim 200 \mu\text{m}$ . The out-of-plane resolution, determined by the cylindrical focusing of the transducer, is  $\sim 1 \text{ mm}$ . To accelerate the imaging speed, an array of ultrasonic transducers in a ring has been adopted<sup>61</sup>.

In planar-view photoacoustic computed tomography, ultrasonic detection follows a plane<sup>34</sup>. Instead of the piezoelectric technique, optical interferometry can be used to sense the ultrasonic displacement<sup>62–65</sup> or pressure<sup>66,67</sup>. A solid planar Fabry–Pérot interferometer was constructed<sup>67,68</sup> and a dielectric or polymer spacer was sandwiched between a pair of mirrors. A focused laser beam was scanned across the surface of the interferometer, and the detected power fluctuation of the reflected laser beam was converted to the optical thickness of the interferometer, which was subsequently converted to pressure. An inverse algorithm was then used to reconstruct a photoacoustic image (Fig. 2b, right)<sup>68,69</sup>.

Optical detection offers three main advantages: first, the optical detector can be made optically transparent, facilitating light delivery to the object for full-field imaging; second, the spatial sampling frequency can be increased without sacrificing sensitivity, allowing high-resolution imaging — sensitivities of tens-of-Pascals have been achieved at a bandwidth of 20 MHz (ref. 67), similar to those of 1-mm-diameter piezoelectric receivers and better than those of smaller diameter receivers; third, the frequency response can be stretched to low frequencies, potentially enabling the interior of a large heterogeneity to be imaged. At present, the technology is limited by system complexity and the read-out speed.

In spherical-view photoacoustic computed tomography, ultrasonic detection follows a truncated spherical surface<sup>70</sup>. In a recently constructed small-animal whole-body photoacoustic tomography system<sup>71</sup>, the animal (a mouse immersed in a coupling liquid) is rotated inside a virtual spherical surface on which a concave arched array of 64 piezo-composite ultrasonic transducers is situated. Two expanded counter-propagating laser beams illuminate the specimen orthogonally to the plane of the array. The internal organs were imaged at a wavelength of 755 nm (Fig. 2c)<sup>71</sup>.

In linear-view photoacoustic computed tomography, ultrasonic detection follows a line<sup>72–77</sup>. Linear ultrasound arrays in medical ultrasound imaging systems can be adapted for PAT. The ultrasound probes are typically handheld and can therefore adapt to various anatomical sites conveniently. In ultrasound imaging, transmission and detection is achieved by switching on certain subsets of the array elements, and shifting the selection subset across the array forms a 2D image. In PAT, the entire array can receive ultrasonic signals simultaneously because photoacoustic excitation usually covers a large volume. Ultrasound and photoacoustic images can, of course, be displayed side-by-side to present complementary imaging contrasts.

Photoacoustic computed tomography can be implemented with linear or planar ultrasonic transducers instead of point detectors<sup>40,78–80</sup>. In this embodiment, the detected signals represent an integration of pressure over cylindrical or planar surfaces with varying distances to each transducer. Planar ultrasonic transduction is of particular interest for two main reasons: first, the forward problem represents a standard Radon transformation — the associated inverse algorithms can be used directly for PAT; second, the spatial resolution is limited only by the ultrasonic bandwidth. In conventional photoacoustic computed tomography, point ultrasonic detectors are approximated by finite-size detectors, resulting in a trade-off between detection sensitivity and lateral resolution. If the detectors are too small the sensitivity is compromised, if they are too large the resolution becomes poor. There is no such compromise in PAT based on planar ultrasonic transducers.

PAT lends itself to breast imaging. Breast tissue has a relatively homogeneous ( $\sim \pm 5\%$ ) speed of sound, and breast tumours tend to

have higher blood concentrations and lower oxygen saturations of haemoglobin than surrounding tissues. Figure 3a shows an *in vivo* photoacoustic image of a human breast<sup>81</sup>, where the ultrasonic detection follows an arc<sup>37</sup>. The imaged lesion measured  $\sim 18 \text{ mm}$  across and was 23 mm below the laser-illumination surface; biopsy confirmed it was an invasive carcinoma. Figure 3b shows another *in vivo* photoacoustic image of a human breast<sup>82</sup>, where the ultrasonic detection follows a plane<sup>83</sup>. The lesion was identified as a ring-shaped structure with an average optical absorption contrast of 1.6, relative to the background. The lesion was estimated to be 30 mm in diameter, comparable to the pathologically estimated size of 26 mm.

### Photoacoustic molecular imaging

PAT is well-suited for molecular imaging — whereas functional imaging is based on endogenous contrast, molecular imaging is based on exogenous contrast (which essentially stains invisible biomarkers *in vivo*). Functional imaging maps physiological activities usually at the tissue or organ level, whereas molecular imaging measures biological and pathophysiological processes at the molecular level. Simultaneous functional and molecular PAT of glioblastoma brain tumours has been demonstrated in live mice<sup>13</sup>. A small-molecule organic dye conjugated with a cyclopeptide serves as the molecular imaging probe to target the biomarker  $\alpha_v\beta_3$  integrin, which tends to be overexpressed in angiogenesis. The functional image shows tumour hypoxia, whereas the molecular image shows tumour over-expression of integrin.

Besides imaging small molecules, PAT can also track various nanoparticles, such as metallic nanoshells<sup>84</sup>, nanorods<sup>10,85–89</sup>, nanocages<sup>90</sup>, carbon nanotubes<sup>9</sup> and dye-embedded nanoparticles<sup>91</sup>. The large optical absorption cross-sections for nanoparticles<sup>92</sup> provide excellent contrast for PAT. Unlike small-molecule organic dyes, nanoparticles resist chemical or thermal denaturation and photobleaching. However, further toxicity studies are required before they can be applied to humans.

The surfaces of gold nanoparticles exhibit good biocompatibility and can accommodate functionalities by conjugating with targeting peptides or antibodies<sup>11,87,93</sup>. So far, biomarkers targeted in PAT include EGFR<sup>11</sup>, HER-2 (ref. 87) and CXCR-4 (ref. 93), which are often overexpressed in breast cancer, as well as ICAM-1, which is involved in inflammatory responses<sup>88</sup>. In metallic nanoparticles, the optical absorption is based on surface plasmon resonance, and the peak absorption wavelength can be tuned throughout the visible and near-infrared spectral region by varying the physical dimensions.

Dye-embedded nanoparticles can also function as an effective contrast agent<sup>91</sup>. Indocyanine green (ICG) is an organic dye that has been approved for human use. It has strong optical absorption around the 800-nm near-infrared wavelength. Although ICG itself has been demonstrated to enhance photoacoustic contrast *in vivo*<sup>94</sup>, the half-life of ICG in the blood stream is only several minutes, limiting the time available for sustained monitoring. Encapsulation of ICG in nanoparticles increases the circulation time significantly<sup>91</sup>. Furthermore, encapsulation provides surfaces for adding functionalities, increases the dye concentration for greater optical absorption, and shields the dye molecules from destabilizing effects due to the biological environment. ICG-embedded nanoparticles conjugated with HER-2 antibodies have been shown to target breast cancer and prostate cancer cells *in vitro*<sup>91</sup>.

Molecular PAT of the *lacZ* reporter gene was demonstrated in small living animals<sup>8</sup>. Reporter gene imaging, a form of molecular imaging, can help us understand the nature of gene expression during *in vivo* development and pathogenesis. Unlike conventional reporter gene imaging (which is based on fluorescent proteins such as the well-known ‘green fluorescent protein’), photoacoustic reporter gene imaging is based on optical absorption that is converted into heat. The *lacZ* gene — one of the most widely used

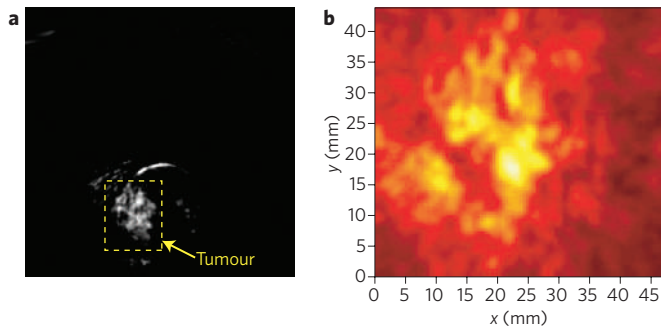


**Figure 3 | In vivo photoacoustic computed tomography of the human breast acquired at 1064-nm laser wavelength.** **a**, Image of a human breast containing a poorly differentiated infiltrating ductal carcinoma. The slice is 21 mm deep from the laser-illumination surface. The field of view is 120 mm  $\times$  120 mm. **b**, Image of a breast containing an invasive ductal carcinoma. The slice is 13.5 mm deep from the laser-illumination surface. Images in **a** and **b** are reproduced from, respectively, ref. 81. © 2009 SPIE; and ref. 82. © 2007 OSA.

reporter genes in biology — encodes the enzyme  $\beta$ -galactosidase. A sensitive chromogenic assay with X-gal — an optically transparent substrate — yields a stable dark blue product that serves as an optical absorption contrast agent for PAT. Because the blue product absorption spectrum peaks at approximately 650 nm, multi-millimetre penetration can be achieved. However, if multi-centimetre penetration is desired, new reporter genes that produce gene-expression products absorbing in the near-infrared spectral region must be developed. By providing high spatial resolution at depths beyond the optical transport mean free path *in vivo*, PAT is expected to become a complementary tool to conventional optical imaging of reporter genes.

PAT is as sensitive as many molecular imaging modalities, although such a comparison depends on many parameters, including its biomedical applications<sup>95</sup>. When intrinsic biological contrasts are sensed (caused, for example, by the presence of red blood cells or melanoma cells), single-cell sensitivity can be achieved<sup>81,55</sup>. When extrinsic small-molecule contrast agents are imaged, PAT can provide a sensitivity of the order of  $\sim 10$  nmol per litre (or  $\sim$ fmol per voxel, where a 'voxel' is a volumetric pixel) at  $\sim 0.3$ -mm resolution<sup>13,96</sup>. Pure optical fluorescence imaging can provide a sensitivity of the order of  $\sim$ nmol per litre (or  $\sim$ fmol per voxel) at  $\sim 1$ -mm resolution<sup>97</sup>: a worse resolution but slightly better sensitivity when compared with PAT. Nuclear imaging such as PET can provide a sensitivity of the order of  $\sim$ pmol per litre (or  $\sim 0.1$  fmol per voxel) at  $\sim 3$ -mm resolution: a much worse resolution but better sensitivity when compared with PAT<sup>98,99</sup>. However, the sensitivity of PAT may be improved by increasing parameters such as the local optical fluence, the optical absorption cross-section of the contrast agent, the number of signals for averaging and the voxel size. For example, when extrinsic nanoshell contrast agents are imaged, PAT can provide a sensitivity of the order of  $\sim 10$  pmol per litre (or  $\sim 0.0001$  fmol per voxel) at  $\sim 0.06$ -mm resolution<sup>84</sup>. Because different modalities have dissimilar imaging capabilities, sensitivity should not be the only parameter when selecting a tool for a particular application. Furthermore, nuclear imaging uses ionizing radiation, whereas PAT and optical fluorescence imaging use non-ionizing radiation.

### Limitations of PAT and outlook

PAT has limitations, as does any imaging technology. First, optical attenuation limits the penetration to  $\sim 5$  cm when a resolution of less than 1 mm is desired in tissue<sup>81,100,101</sup>. Microwaves or radio waves can be used for deeper excitation, although the contrast origins differ. Second, ultrasound sustains strong reflection from

gas–liquid or gas–solid interfaces, owing to the strong mismatch of acoustic impedances. Therefore, ultrasound signals cannot penetrate through gas cavities or lung tissues efficiently. For the same reason, ultrasonic detection requires direct contact between the ultrasonic transducers and the biological tissue. Usually, ultrasound coupling gel is applied to the tissue surface to remove intervening air cavities. The development of non-contact optical detection for acoustic displacement is a potential solution to this problem<sup>62–65</sup>. Third, ultrasound suffers from significant attenuation and phase distortion in thick bones, such as the human skull. Fortunately, unlike pulse-echo ultrasound imaging, PAT involves only one-way ultrasound attenuation through the skull. Sufficiently strong photoacoustic signals have been observed through Rhesus monkey skulls<sup>102,103</sup>. The remaining challenge is to compensate for the phase distortion introduced by the skull.

Research on PAT has gained significant momentum recently: the number of research articles on PAT has more than tripled since 2003 (Source: Science Citation Index. Search criteria: Topic=((photoacoustic or optoacoustic) and (imaging or tomography or microscopy)) AND Document Type=(Article); ref. 104). PAT is expected to find broad applications in both biology and medicine. As a result, there are many potential *in vivo* applications that may come to fruition in the near future: melanoma detection<sup>32,53,56,58</sup>, intravascular catheter imaging<sup>105–107</sup>, endoscopic imaging, simultaneous functional and molecular imaging<sup>13</sup>, reporter gene imaging<sup>8</sup>, sentinel lymph node mapping<sup>50,59</sup>, breast imaging<sup>81,82,108–110</sup> and multi-scale imaging.

### References

- Oraevsky, A. A. & Karabutov, A. A. in *Biomedical Photonics Handbook* Vol. PM125 (ed. Vo-Dinh, T.) Ch. 34, 3401–3434 (CRC Press, 2003).
- Xu, M. H. & Wang, L. V. Photoacoustic imaging in biomedicine. *Rev. Sci. Instrum.* **77**, 041101 (2006).
- Wang, L. V. (ed.) *Photoacoustic Imaging and Spectroscopy* (CRC Press, 2009).
- Wang, X. D. *et al.* Noninvasive laser-induced photoacoustic tomography for structural and functional *in vivo* imaging of the brain. *Nature Biotechnol.* **21**, 803–806 (2003).
- Siphanto, R. I. *et al.* Serial noninvasive photoacoustic imaging of neovascularization in tumor angiogenesis. *Opt. Express* **13**, 89–95 (2005).
- Laufer, J., Delpy, D., Elwell, C. & Beard, P. Quantitative spatially resolved measurement of tissue chromophore concentrations using photoacoustic spectroscopy: application to the measurement of blood oxygenation and haemoglobin concentration. *Phys. Med. Biol.* **52**, 141–168 (2007).
- Yang, S., Xing, D., Zhou, Q., Xiang, L. & Lao, Y. Functional imaging of cerebrovascular activities in small animals using high-resolution photoacoustic tomography. *Med. Phys.* **34**, 3294–3301 (2007).
- Li, L., Zemp, R. J., Lungu, G., Stoica, G. & Wang, L. V. Photoacoustic imaging of lacZ gene expression *in vivo*. *J. Biomed. Opt.* **12**, 020504 (2007).
- De La Zerda, A. *et al.* Carbon nanotubes as photoacoustic molecular imaging agents in living mice. *Nature Nanotechnol.* **3**, 557–562 (2008).
- Copland, J. A. *et al.* Bioconjugated gold nanoparticles as a molecular based contrast agent: Implications for imaging of deep tumors using optoacoustic tomography. *Mol. Imaging Biol.* **6**, 341–349 (2004).
- Mallidi, S., Larson, T., Aaron, J., Sokolov, K. & Emelianov, S. Molecular specific optoacoustic imaging with plasmonic nanoparticles. *Opt. Express* **15**, 6583–6588 (2007).
- Razansky, D. & Ntziachristos, V. Hybrid photoacoustic fluorescence molecular tomography using finite-element-based inversion. *Med. Phys.* **34**, 4293–4301 (2007).
- Li, M.-L. *et al.* Simultaneous molecular and hypoxia imaging of brain tumors *in vivo* using spectroscopic photoacoustic tomography. *Proc. IEEE* **96**, 481–489 (2008).
- Bell, A. G. On the production and reproduction of sound by light. *Am. J. Sci.* **20**, 305–324 (1880).
- Bowen, T. Radiation-induced thermoacoustic imaging. US patent 4,385,634 (1983).
- Oraevsky, A. A., Jacques, S. L. & Tittel, F. K. Determination of tissue optical properties by piezoelectric detection of laser-induced stress waves. *Proc. SPIE* **1882**, 86–101 (1993).
- Oraevsky, A. A., Jacques, S. L., Esenaliev, R. O. & Tittel, F. K. Laser-based optoacoustic imaging in biological tissues. *Proc. SPIE* **2134A**, 122–128 (1994).
- Kruger, R. A. Photoacoustic ultrasound. *Med. Phys.* **21**, 127–131 (1994).

19. Kruger, R. A. & Liu, P. Photoacoustic ultrasound: pulse production and detection in 0.5% liposyn. *Med. Phys.* **21**, 1179–1184 (1994).
20. Oraevsky, A. A., Esenaliev, R. O., Jacques, S. L., Thomsen, S. L. & Tittel, F. K. Lateral and z-axial resolution in laser photoacoustic imaging with ultrasonic transducers. *Proc. SPIE* **2389**, 198–208 (1995).
21. Kruger, R. A., Liu, P., Fang, Y. R. & Appledorn, C. R. Photoacoustic ultrasound (PAUS) — reconstruction tomography. *Med. Phys.* **22**, 1605–1609 (1995).
22. Ku, G. & Wang, L. V. Scanning thermoacoustic tomography in biological tissue. *Med. Phys.* **27**, 1195–1202 (2000).
23. Yang, S. *et al.* Noninvasive monitoring of traumatic brain injury and post-traumatic rehabilitation with laser-induced photoacoustic imaging. *Appl. Phys. Lett.* **90**, 243902 (2007).
24. Zhang, Q. *et al.* Non-invasive imaging of epileptic seizures *in vivo* using photoacoustic tomography. *Phys. Med. Biol.* **53**, 1921–1931 (2008).
25. Betzig, E. *et al.* Imaging intracellular fluorescent proteins at nanometer resolution. *Science* **313**, 1642–1645 (2006).
26. Hell, S. W. Far-field optical nanoscopy. *Science* **316**, 1153–1158 (2007).
27. Huang, B., Wang, W., Bates, M. & Zhuang, X. Three-dimensional super-resolution imaging by stochastic optical reconstruction microscopy. *Science* **319**, 810–813 (2008).
28. Wang, L. V. & Wu, H. *Biomedical Optics: Principles and Imaging* (Wiley, 2007).
29. Wang, L. V., Zhao, X., Sun, H. & Ku, G. Microwave-induced acoustic imaging of biological tissues. *Rev. Sci. Instrum.* **70**, 3744–3748 (1999).
30. Kruger, R. A., Reinecke, D. R. & Kruger, G. A. Thermoacoustic computed tomography—technical considerations. *Med. Phys.* **26**, 1832–1837 (1999).
31. Guo, Z., Li, L. & Wang, L. V. The speckle-free nature of photoacoustic tomography. *Proc. SPIE* **7177**, 71772J (2009).
32. Zhang, H. F., Maslov, K., Stoica, G. & Wang, L. V. Functional photoacoustic microscopy for high-resolution and noninvasive *in vivo* imaging. *Nature Biotechnol.* **24**, 848–851 (2006).
33. Zhang, H. F., Maslov, K. & Wang, L. V. *In vivo* imaging of subcutaneous structures using functional photoacoustic microscopy. *Nature Protoc.* **2**, 797–804 (2007).
34. Hoelen, C. G. A., de Mul, F. F. M., Pongers, R. & Dekker, A. Three-dimensional photoacoustic imaging of blood vessels in tissue. *Opt. Lett.* **23**, 648–650 (1998).
35. Kostli, K. P. *et al.* Photoacoustic imaging using a three-dimensional reconstruction algorithm. *IEEE J. Sel. Top. Quant.* **7**, 918–923 (2001).
36. Paltauf, G., Viator, J. A., Prael, S. A. & Jacques, S. L. Iterative reconstruction algorithm for photoacoustic imaging. *J. Acoust. Soc. Am.* **112**, 1536–1544 (2002).
37. Andreev, V. G., Karabutov, A. A. & Oraevsky, A. A. Detection of ultrawide-band ultrasound pulses in photoacoustic tomography. *IEEE T. Ultrason. Ferr.* **50**, 1383–1390 (2003).
38. Finch, D., Patch, S. K. & Rakesh. Determining a function from its mean values over a family of spheres. *SIAM J. Math. Anal.* **35**, 1213–1240 (2003).
39. Kostli, K. P. & Beard, P. C. Two-dimensional photoacoustic imaging by use of Fourier-transform image reconstruction and a detector with an anisotropic response. *Appl. Opt.* **42**, 1899–1908 (2003).
40. Haltmeier, M., Scherzer, O., Burgholzer, P. & Paltauf, G. Thermoacoustic computed tomography with large planar receivers. *Inverse Probl.* **20**, 1663–1673 (2004).
41. Xu, M. & Wang, L. V. Universal back-projection algorithm for photoacoustic computed tomography. *Phys. Rev. E* **71**, 016706 (2005).
42. Cox, B. T. & Beard, P. C. Fast calculation of pulsed photoacoustic fields in fluids using *k*-space methods. *J. Acoust. Soc. Am.* **117**, 3616–3627 (2005).
43. Cox, B. T., Arridge, S. R., Köstli, K. P. & Beard, P. C. Two-dimensional quantitative photoacoustic image reconstruction of absorption distributions in scattering media by use of a simple iterative method. *Appl. Opt.* **45**, 1866–1875 (2006).
44. Anastasio, M. A., Zhang, J., Modgil, D. & La Rivière, P. J. Application of inverse source concepts to photoacoustic tomography. *Inverse Probl.* **23**, S21–S35 (2007).
45. Hoelen, C. G. A. & de Mul, F. F. M. Image reconstruction for photoacoustic scanning of tissue structures. *Appl. Opt.* **39**, 5872–5883 (2000).
46. Köstli, K. P., Frenz, M., Bebie, H. & Weber, H. P. Temporal backward projection of photoacoustic pressure transients using Fourier transform methods. *Phys. Med. Biol.* **46**, 1863–1872 (2001).
47. Larina, I. V., Larin, K. V. & Esenaliev, R. O. Real-time photoacoustic monitoring of temperature in tissues. *J. Phys. D Appl. Phys.* **38**, 2633–2639 (2005).
48. Sethuraman, S., Aglyamov, S. R., Smalling, R. W. & Emelianov, S. Y. Remote temperature estimation in intravascular photoacoustic imaging. *Ultrasound Med. Biol.* **34**, 299–308 (2008).
49. Shah, J. *et al.* Photoacoustic imaging and temperature measurement for photothermal cancer therapy. *J. Biomed. Opt.* **13**, 034024 (2008).
50. Song, K. H., Stein, E. W., Margenthaler, J. A. & Wang, L. V. Noninvasive photoacoustic identification of sentinel lymph nodes containing methylene blue *in vivo* in a rat model. *J. Biomed. Opt.* **13**, 054033 (2008).
51. Maslov, K., Zhang, H. F., Hu, S. & Wang, L. V. Optical-resolution photoacoustic microscopy for *in vivo* imaging of single capillaries. *Opt. Lett.* **33**, 929–931 (2008).
52. Savateeva, E. V. *et al.* Noninvasive detection and staging of oral cancer *in vivo* with confocal photoacoustic tomography. *Proc. SPIE* **3916**, 55–66 (2000).
53. Galanzha, E. I., Shashkov, E. V., Tuchin, V. V. & Zharov, V. P. *In vivo* multispectral, multiparameter, photoacoustic lymph flow cytometry with natural cell focusing, label-free detection and multicolor nanoparticle probes. *Cytom. Part A* **73A**, 884–894 (2008).
54. Olszewski, W. L. & Tárnok, A. Photoacoustic listening of cells in lymphatics: Research art or novel clinical noninvasive lymph test. *Cytom. Part A* **73A**, 1111–1113 (2008).
55. Zharov, V. P., Galanzha, E. I., Shashkov, E. V., Khlebtsov, N. G. & Tuchin, V. V. *In vivo* photoacoustic flow cytometry for monitoring of circulating single cancer cells and contrast agents. *Opt. Lett.* **31**, 3623–3625 (2006).
56. Weight, R. M., Viator, J. A., Dale, P. S., Caldwell, C. W. & Lisle, A. E. Photoacoustic detection of metastatic melanoma cells in the human circulatory system. *Opt. Lett.* **31**, 2998–3000 (2006).
57. Zharov, V. P. *et al.* Photoacoustic flow cytometry: principle and application for real-time detection of circulating single nanoparticles, pathogens, and contrast dyes *in vivo*. *J. Biomed. Opt.* **12**, 051503 (2007).
58. Holan, S. H. & Viator, J. A. Automated wavelet denoising of photoacoustic signals for circulating melanoma cell detection and burn image reconstruction. *Phys. Med. Biol.* **53**, N227–N236 (2008).
59. Ambartsoumian, G. & Kuchment, P. On the injectivity of the circular Radon transform. *Inverse Probl.* **21**, 473–485 (2005).
60. Haltmeier, M., Scherzer, O., Burgholzer, P., Nuster, R. & Paltauf, G. Thermoacoustic tomography and the circular Radon transform: Exact inversion formula. *Math. Mod. Meth. Appl. Sci.* **17**, 635–655 (2007).
61. Gamelin, J. *et al.* Curved array photoacoustic tomographic system for small animal imaging. *J. Biomed. Opt.* **13**, 024007 (2008).
62. Hamilton, J. D. & O'Donnell, M. High frequency ultrasound imaging with optical arrays. *IEEE T. Ultrason. Ferr.* **45**, 216–235 (1998).
63. Payne, B. P., Venugopalan, V., Mikić, B. B. & Nishioka, N. S. Photoacoustic tomography using time-resolved interferometric detection of surface displacement. *J. Biomed. Opt.* **8**, 273–280 (2003).
64. Carp, S. A., Guerra, A., Duque, S. Q. & Venugopalan, V. Photoacoustic imaging using interferometric measurement of surface displacement. *Appl. Phys. Lett.* **85**, 5772–5774 (2004).
65. Carp, S. A. & Venugopalan, V. Photoacoustic imaging based on the interferometric measurement of surface displacement. *J. Biomed. Opt.* **12**, 064001 (2007).
66. Beard, P. C., Perennes, F. & Mills, T. N. Transduction mechanisms of the Fabry-Perot polymer film sensing concept for wideband ultrasound detection. *IEEE T. Ultrason. Ferr.* **46**, 1575–1582 (1999).
67. Zhang, E., Laufer, J. & Beard, P. Backward-mode multiwavelength photoacoustic scanner using a planar Fabry-Perot polymer film ultrasound sensor for high-resolution three-dimensional imaging of biological tissues. *Appl. Opt.* **47**, 561–577 (2008).
68. Laufer, J., Zhang, E., Raivich, G. & Beard, P. Three-dimensional noninvasive imaging of the vasculature in the mouse brain using a high resolution photoacoustic scanner. *Appl. Opt.* **48**, D299–D306 (2009).
69. Zhang, E. Z., Laufer, J. G., Pedley, R. B. & Beard, P. C. *In vivo* high-resolution 3D photoacoustic imaging of superficial vascular anatomy. *Phys. Med. Biol.* **54**, 1035–1046 (2009).
70. Kruger, R. A., Kiser, W. L., Reinecke, D. R., Kruger, G. A. & Miller, K. D. Thermoacoustic molecular imaging of small animals. *Mol. Imaging* **2**, 113–123 (2003).
71. Brecht, H.-P. *et al.* Photoacoustic 3D whole-body tomography: experiments in nude mice. *Proc. SPIE* **7177**, 71770E (2009).
72. Kruger, R. A., Kiser, W. L., Reinecke, D. R. & Kruger, G. A. Thermoacoustic computed tomography using a conventional linear transducer array. *Med. Phys.* **30**, 856–860 (2003).
73. Zeng, Y., Xing, D., Wang, Y., Yin, B. & Chen, Q. Photoacoustic and ultrasonic coimage with a linear transducer array. *Opt. Lett.* **29**, 1760–1762 (2004).
74. Yin, B. *et al.* Fast photoacoustic imaging system based on 320-element linear transducer array. *Phys. Med. Biol.* **49**, 1339–1346 (2004).
75. Niederhauser, J. J., Jaeger, M., Lemor, R., Weber, P. & Frenz, M. Combined ultrasound and photoacoustic system for real-time high-contrast vascular imaging *in vivo*. *IEEE T. Med. Imaging* **24**, 436–440 (2005).
76. Yang, D. W., Xing, D., Yang, S. H. & Xiang, L. Z. Fast full-view photoacoustic imaging by combined scanning with a linear transducer array. *Opt. Express* **15**, 15566–15575 (2007).
77. Nie, L., Xing, D., Yang, D., Zeng, L. & Zhou, Q. Detection of foreign body using fast thermoacoustic tomography with a multielement linear transducer array. *Appl. Phys. Lett.* **90**, 174109 (2007).

78. Burgholzer, P., Hofer, C., Paltauf, G., Haltmeier, M. & Scherzer, O. Thermoacoustic tomography with integrating area and line detectors. *IEEE T. Ultrason. Ferr.* **52**, 1577–1583 (2005).
79. Burgholzer, P., Bauer-Marschallinger, J., Grün, H., Haltmeier, M. & Paltauf, G. Temporal back-projection algorithms for photoacoustic tomography with integrating line detectors. *Inverse Probl.* **23**, S65–S80 (2007).
80. Paltauf, G., Nuster, R., Haltmeier, M. & Burgholzer, P. Experimental evaluation of reconstruction algorithms for limited view photoacoustic tomography with line detectors. *Inverse Probl.* **23**, S81–S94 (2007).
81. Ermilov, S. A. *et al.* Laser optoacoustic imaging system for detection of breast cancer. *J. Biomed. Opt.* **14**, 024007 (2009).
82. Manohar, S. *et al.* Initial results of *in vivo* non-invasive cancer imaging in the human breast using near-infrared photoacoustics. *Opt. Express* **15**, 12277–12285 (2007).
83. Manohar, S., Kharine, A., van Hespren, J. C. G., Steenbergen, W. & van Leeuwen, T. G. The Twente Photoacoustic Mammoscope: system overview and performance. *Phys. Med. Biol.* **50**, 2543–2557 (2005).
84. Wang, Y. *et al.* Photoacoustic tomography of a nanoshell contrast agent in the *in vivo* rat brain. *Nano Lett.* **4**, 1689–1692 (2004).
85. Li, P.-C. *et al.* Photoacoustic flow measurements by use of laser-induced shape transitions of gold nanorods. *Opt. Lett.* **30**, 3341–3343 (2005).
86. Eghtedari, M. *et al.* High sensitivity of *in vivo* detection of gold nanorods using a laser optoacoustic imaging system. *Nano Lett.* **7**, 1914–1918 (2007).
87. Agarwal, A. *et al.* Targeted gold nanorod contrast agent for prostate cancer detection by photoacoustic imaging. *J. Appl. Phys.* **102**, 064701 (2007).
88. Kim, K. *et al.* Photoacoustic imaging of early inflammatory response using gold nanorods. *Appl. Phys. Lett.* **90**, 223901 (2007).
89. Chamberland, D. L. *et al.* Photoacoustic tomography of joints aided by an Etanercept-conjugated gold nanoparticle contrast agent — an *ex vivo* preliminary rat study. *Nanotechnology* **19**, 095101 (2008).
90. Yang, X., Skrabalak, S. E., Li, Z.-Y., Xia, Y. & Wang, L. V. Photoacoustic tomography of a rat cerebral cortex *in vivo* with Au nanocages as an optical contrast agent. *Nano Lett.* **7**, 3798–3802 (2007).
91. Kim, G. *et al.* Indocyanine-green-embedded PEBBLES as a contrast agent for photoacoustic imaging. *J. Biomed. Opt.* **12**, 044020 (2007).
92. Hu, M. *et al.* Gold nanostructures: engineering their plasmonic properties for biomedical applications. *Chem. Soc. Rev.* **35**, 1084–1094 (2006).
93. Li, P.-C. *et al.* Photoacoustic imaging of multiple targets using gold nanorods. *IEEE T. Ultrason. Ferr.* **54**, 1642–1647 (2007).
94. Wang, X. *et al.* Noninvasive photoacoustic angiography of animal brains *in vivo* with near-infrared light and an optical contrast agent. *Opt. Lett.* **29**, 730–732 (2004).
95. Razansky, D., Baeten, J. & Ntziachristos, V. Sensitivity of molecular target detection by multispectral optoacoustic tomography (MSOT). *Med. Phys.* **36**, 939–945 (2009).
96. Razansky, D., Vinegoni, C. & Ntziachristos, V. Multispectral photoacoustic imaging of fluorochromes in small animals. *Opt. Lett.* **32**, 2891–2893 (2007).
97. Ntziachristos, V., Ripoll, J., Wang, L. V. & Weissleder, R. Looking and listening to light: the evolution of whole-body photonic imaging. *Nature Biotechnol.* **23**, 313–320 (2005).
98. Phelps, M. E. PET: A biological imaging technique. *Neurochem. Res.* **16**, 929–940 (1991).
99. MacLaren, D. C. *et al.* PET imaging of transgene expression. *Biol. Psychiat.* **48**, 337–348 (2000).
100. Esenaliev, R. O., Karabutov, A. A. & Oraevsky, A. A. Sensitivity of laser optoacoustic imaging in detection of small deeply embedded tumors. *IEEE J. Sel. Top. Quant.* **5**, 981–988 (1999).
101. Ku, G. & Wang, L. V. Deeply penetrating photoacoustic tomography in biological tissues enhanced with an optical contrast agent. *Opt. Lett.* **30**, 507–509 (2005).
102. Xu, Y. & Wang, L. V. Rhesus monkey brain imaging through intact skull with thermoacoustic tomography. *IEEE T. Ultrason. Ferr.* **53**, 542–548 (2006).
103. Yang, X. & Wang, L. V. Monkey brain cortex imaging by photoacoustic tomography. *J. Biomed. Opt.* **13**, 044009 (2008).
104. <http://www.isiknowledge.com>
105. Sethuraman, S., Amirian, J. H., Litovsky, S. H., Smalling, R. W. & Emelianov, S. Y. *Ex vivo* characterization of atherosclerosis using intravascular photoacoustic imaging. *Opt. Express* **15**, 16657–16666 (2007).
106. Sethuraman, S., Aglyamov, S. R., Amirian, J. H., Smalling, R. W. & Emelianov, S. Y. Intravascular photoacoustic imaging using an IVUS imaging catheter. *IEEE T. Ultrason. Ferr.* **54**, 978–986 (2007).
107. Sethuraman, S., Amirian, J. H., Litovsky, S. H., Smalling, R. W. & Emelianov, S. Y. Spectroscopic intravascular photoacoustic imaging to differentiate atherosclerotic plaques. *Opt. Express* **16**, 3362–3367 (2008).
108. Oraevsky, A. A. *et al.* Initial clinical evaluation of laser optoacoustic imaging system for diagnostic imaging of breast cancer. *Breast Cancer Res. Tr.* **106**, S47 (2007).
109. Manohar, S., Kharine, A., van Hespren, J. C. G., Steenbergen, W. & van Leeuwen, T. G. Photoacoustic mammography laboratory prototype: imaging of breast tissue phantoms. *J. Biomed. Opt.* **9**, 1172–1181 (2004).
110. Kruger, R. A. *et al.* Breast cancer *in vivo*: Contrast enhancement with thermoacoustic CT at 434 MHz — feasibility study. *Radiology* **216**, 279–283 (2000).

### Acknowledgements

The author acknowledges the support by the National Institutes of Health Grants R01 EB000712, R01 NS046214, R01 EB008085 and U54 CA136398. Thanks to Song Hu for providing Fig. 1d.

### Additional information

The author declares competing financial interests: details accompany the full-text HTML version of the paper at [www.nature.com/naturephotonics](http://www.nature.com/naturephotonics).